Influences of Nano-structured Thermal Stability on the Intergranular Corrosion of High-Carbon Austenitic Heat-Resistant Steel

LingMin Yao and RuiKun Wang

The influences of nano-structured thermal stability on the intergranular corrosion (IGC) of Super304H steel were investigated by electrochemical tests and surface analysis in this study. It was found that IGC in nano-twinned (NT) Super304H SS during the aging process was governed by the formation of nano-scale $M_{23}C_6$ precipitates, which generated Cr-depletion zones, and fast healing of the Cr-depletion zones due to the rapid infusion of Cr atoms from the matrix. Conversely, the nano-grains (NG) with poor thermal stability could accelerate the nucleation of sigma phase at recrystallizing interfaces after short-time aging at 650 °C, thereby deteriorating the IGC resistance. The thermal stability of the NT structure was superior to that of the NG structure, which preserved the IGC resistance of Super304H SS during the aging process. Therefore, it was critical to keep the SP strain below the saturation value to achieve high thermal stability, good IGC resistance, and suppression of recrystallisation-induced precipitation.

1. Introduction

Super304H stainless steel (Super304H SS) has been widely used in advanced ultra-supercritical (A-USC) or ultra-super-critical (USC) power plants because of its combination of desirable elevated-temperature strength (Ref 1, 2) and oxidation resistance (Ref 3, 4). However, a contradiction between enhancement of the elevated-temperature strength via increasing C content (Ref 5, 6) and intergranular corrosion (IGC) owing to the precipitation of chromium-rich carbides (Ref 7) as it is exposed to operation temperature of 600-700 °C is the issue for austenitic heat-resistant steel, which has not yet been solved.

Most of the works focused on the mechanical properties including high-temperature strength and creep resistance of Super304H SS (Ref 8-13). However, research (Ref 7, 14-16) on the susceptibility to IGC of Super304H SS is rare. The conventional methods, such as solution treatments, high-temperature softening (Ref 7), and adding carbide forming elements (Ref 17), failed to solve the problem of high intergranular corrosion susceptibility (IGCS) in Super304H SS because it is hard to avoid the precipitation of chromium carbides, and thereby causes Cr-depleted zones around the

carbides at the operating temperature. In our recent works, the rapid diffusion of Cr atoms in the nano-crystalline Super304H SS was found to significantly accelerate the elimination of Cr-depleted zones around carbides (Ref 15, 18). It is expected that the nano-structure with high Cr diffusion rate may result in the fast healing of the Cr-depleted areas and ultimately improving the IGC resistance of Super304H SS at elevated temperatures.

However, the application of high-diffusion nano-crystalline (NC) materials induced by plastic deformation in high-temperature condition is challenging because NC materials with high excess energy usually have poor thermal stability (Ref 19, 20). Alternatively, nano-twinned material, inside which twin boundaries (TBs) are spaced several or tens of nanometers apart, has become a focus of research for their novel properties including superior thermal stability and IGC resistance (Ref 21-23). To date, several studies (Ref 21, 24, 25) have shown that the thermal stability of nano-twins (NT) is superior to their NC counterparts owing to the low excess energy of deformed TBs. Although the stored energy of the TBs could be increased by introducing high density of dislocations, which is still far lower than that of high-angle grain boundaries (GBs) (Ref 26). For instance, in austenitic stainless steel, NT remains stable up to 800 °C, but nano-grains (NG) start to grow up at 600 °C (Ref 27). The superior thermal stability of the NT reveals the applications of these materials at relatively high temperatures. It is worth noting that the recent discoveries have shown that NT or high-density twinned structures induced by plastic deformation (Ref 22, 23) were succeeded in suppressing sensitization of austenitic stainless steels after sensitized at 750 °C for 48 h or 650 °C for 2 h, respectively, both due to the inhibition of carbide precipitation along TBs emitted at GBs. In a word, the deformed TBs can not only significantly improve the thermal stability of austenitic stainless steels but also effectively suppress the precipitation of chromium carbides at their sensitization temperature. These findings provide a new idea to improve the IGC resistance at elevated temperature, i.e., by introducing substantially deformed NT which could be achieved at sufficiently high-strain rates (Ref 28). Although

LingMin Yao, School of Physics and Electronic Engineering, Guangzhou University, 230 Wai Huan Xi Road, Guangzhou Higher Education Mega Center, Guangzhou 510006, People's Republic of China; and **RuiKun Wang**, School of Mechanical and Electrical Engineering, Guangzhou University, Guangzhou 510006, People's Republic of China. Contact e-mail: wrk2010@163.com.

the thermal stability of nano-structure materials is then the key factor (Ref 29), little is known about its effects on IGC resistance in austenitic stainless steel, especially, for the high-carbon Super304H SS.

In the present paper, the thermal stability of two nano-structures, nano-grains, and nano-twins was focused in the high-carbon austenitic Super304H SS at its operating temperature of 650 °C, and its influence on IGC resistance was investigated. The two kinds of nano-structured samples were obtained in the same shot-peened (SP) Super304H SS but at different depths with different strain levels. Nano-structures and precipitation were investigated using scanning electron microscope (SEM) and transmission electron microscope (TEM). The intergranular corrosion behavior of two nano-structured samples was investigated, compared with the solution-treated sample. The surface morphologies of the samples after IGC tests were characterized.

2. Experimental Details

2.1 Material and Heat Treatments

The material investigated in this study was solution-treated Super304H SS sheet with a thickness of 5 mm. The chemical composition of the steel is given in Table 1. The surfaces of solution-treated Super304H SS samples were treated by high-rate SP (Ref 15). The aging treatments were performed at 650 °C for 0-168 h to overlap the sensitized and self-healing process. Detailed processing parameters and heat treatments are given in Table 2. Two types of SPed samples without or with aging treatment were carefully prepared by mechanical polishing 50 and 200 μm depth from the surface, referred to as NG-50 μm and NT-200 μm, respectively.

2.2 Microstructural Observation and IGC Tests

The samples used for microstructure and precipitate distribution analysis were etched in Villella's reagent (1 g picric acid + 5 mL HCl + 100 mL ethanol) for 60-90 s and observed by field emission SEM (FESEM Zeiss Supra-40) and TEM (JEM-2100 operated at 200 kV) with energy dispersive spectroscopy (EDS). TEM samples were ground firstly using various abrasive papers and then mechanical polished with diamond paste to 80 μm. The samples were finally thinned by twin-jet electro-polishing in a 10 vol.% perchloric acid and 90 vol.% ethanol solution at − 25 °C and at 30 V using a Struers Tenupol 5 device.

The double loop electrochemical potentiokinetic reactivation (DL-EPR) is an effective method to evaluate the intergranular corrosion behavior of sensitized stainless steels (Ref 30). All DL-EPR tests were performed under the same conditions (in 0.5 M H_2SO_4 + 0.01 M KSCN solution at 35 °C) on an electrochemical workstation (Metrohem Autolab) using an saturated calomel reference electrode (SCE) and a platinum foil counter electrode. Each sample, acting as working electrode, was embedded and sealed with cold-curing epoxy resin with an exposure area of 1 cm^2 as to avoid crevice corrosion.

After a 15 min open circuit potential (OCP) measurement, the anodic potential sweep in the DL-EPR test was started from OCP and reversed at + 0.30 V at a scan rate of 1.67 mV/s. Usually, the degree of sensitization (DOS) of investigated samples was evaluated by measuring the ratio of maximum current density of the reverse scan (i_r) to that in the forward scan (i_a) from the respective DL-EPR curve. According to the literature (Ref 31), if two peaks of reactivation current are found in the DL-EPR test, charge ratio of DL-EPR curve is more appropriate, representing the dissolution occurring in the chromium depletion regions contacting to the testing solution. Therefore, the DOS values in this study were calculated using the ratio of the charge of reactivation (Q_r) to the charge of activation (Q_a):

$$R_r = (Q_r/Q_a) \times 100\% \tag{Eq 1}$$

The value of Q_r/Q_a was calculated automatically by using integral area under the reactivation/activation curves in the DL-EPR testing software of Autolab PGSTAT30 advanced potentiostat. Working surface of the sample was observed by SEM after the test. All the experiments were repeated four times to ensure reproducibility.

Table 1 Chemical composition of Super304H steel (wt.%)

C	Si	Mn	Cr	Ni	S	P	Cu	Nb	N	Mo	Al	Fe
0.104	0.02	0.59	18.15	8.51	< 0.005	0.030	3.04	0.42	0.11	0.25	0.012	Bal.

Table 2 The parameters of heat treatments and shot peening treatment

Sample name	Solution treatment	Shot peening	Aging treatment
Solution-treated sample	1150 °C × 0.5 h + water quenched	…	650 °C × (0, 0.02, 0.05, 0.1, 1, 4, 24, 48, 96, 168 h) + water quenched
NG-50 μm sample	…	0.6 MPa/15 min	
NT-200 μm sample			

3. Results

3.1 Microstructures

In this paper, the primary microstructure varies from nano-twins to nano-grains with increasing strain level, which resulted in the distinct thermal stability in two kinds of nano-structured samples. Moreover, main precipitates transformed from the nano-scale $M_{23}C_6$ carbide in the NT-200 μm sample to the coarsening σ-phase plus some $M_{23}C_6$ carbides in the NG-50 μm sample after aging at 650 °C for different time. The evidence of these transformations would be elaborated in following subsections.

3.1.1 Nano-grains in NG-50 μm Sample and Nano-twins in NT-200 μm Sample.
Figure 1(a) shows the depth-dependent gradient microstructure of the deformation layer on the shot-peened sample, which could be observed by SEM after etching the cross-section surface. The grains in the region at a depth of 50 μm are mainly ultrafine grains, as shown in Fig. 1(b). On the contrary, the region at a depth of 200 μm shows a great number of intersected shear bands with main spacing much less than 1 μm, as shown in Fig. 1(c). A remarkable distinction between microstructures formed at 50 and 200 μm depth from the surface of the SPed sample indicates that the refinement mechanism varies with the strain levels.

To distinguish more clearly the microstructures of the NG-50 μm and NT-200 μm sample, TEM was adopted for analysis, as shown in Fig. 2. Twinning is the main mechanism for grain refinement of Super304H SS at the beginning and early stage of the high-rate SP process. Hence, a mixed microstructure of nano-scale twin with large numbers of dislocations and austenite lamellae were formed on the surface of NT-200 μm sample (Fig. 2a), indicated by the corresponding selected-area electron diffraction (SAED) pattern shown in Fig. 2(b). Statistical TEM measurements demonstrated that the thickness of twin/matrix lamellar ranges from a few nano-meters to 55 nm, with an average value of 30 nm. At the high-strain level, when the twinning reaches a certain volume fraction, it becomes saturated due to strain hardening, and the deformation is controlled by dislocation slip. A similar situation in AISI-304 stainless steel has already been reported and the mechanism of deformation has been discussed by other researcher (Ref 32). Therefore, in contrast to the nano-twinned structure of the NT-200 μm sample, the NG-50 μm one possesses more complex nano-scale dislocation structure (Fig. 2c), which is mainly austenite and a small fraction of α′-martensite, indicated by the inset corresponding SAED pattern in Fig. 2(d). Figure 2(d) is the TEM dark-field image of Fig. 2(c), showing the equiaxed grains of γ-austenite with a mean grain size of 22 nm. Therefore, the main microstructure varies from the NT in the NT-200 μm sample to the NG in the NG-50 μm sample with the increase of strain level, following the grain refinement mechanism changes from twinning to dislocation slip.

3.1.2 Microstructures of the Aged NG-50 μm and NT-200 μm Samples.
Subsequent aging of the NT-200 μm sample at 650 °C for 1 h resulted in the formation of a large number of ultra-fine precipitates along deformation bands and original GBs, as shown in Fig. 3(a). Compared to the aged NT-200 μm sample, a more homogeneous and greater number of precipitates can be observed in the aged NG-50 μm sample in Fig. 3(b). With increasing aging time to 24 h, the amount of precipitate along TB is much greater than that of original GBs in aged NT-200 μm samples, as shown in the Fig. 3(c). Meanwhile, the twin/matrix lamellar spacing slightly thickens after aging. Moreover, the volume fractions of the NT bundles and dislocation structures are little changed in this process. However, besides the $M_{23}C_6$ carbides, some larger precipitates σ-phase appeared in the aged NG-50 μm samples, as shown in the Fig. 3(d). More detailed observations on the microstructures and precipitates of the NT-200 μm and NG-50 μm samples after aged for 24 h were made by TEM, as shown in Fig. 4 and 5, respectively.

Figure 4(a) shows a TEM bright-field image of the lath-shaped M23C6 carbide along TBs. The SAED pattern of Fig. 4(a), indexed in Fig. 4(b), shows composite diffractions of $M_{23}C_6$ carbide, γ-austenite and deformation twins with the zone axis: $[011]_{M23C6}//[011]_\gamma//[011]_{twins}$. Figure 4(c) and (d) are the
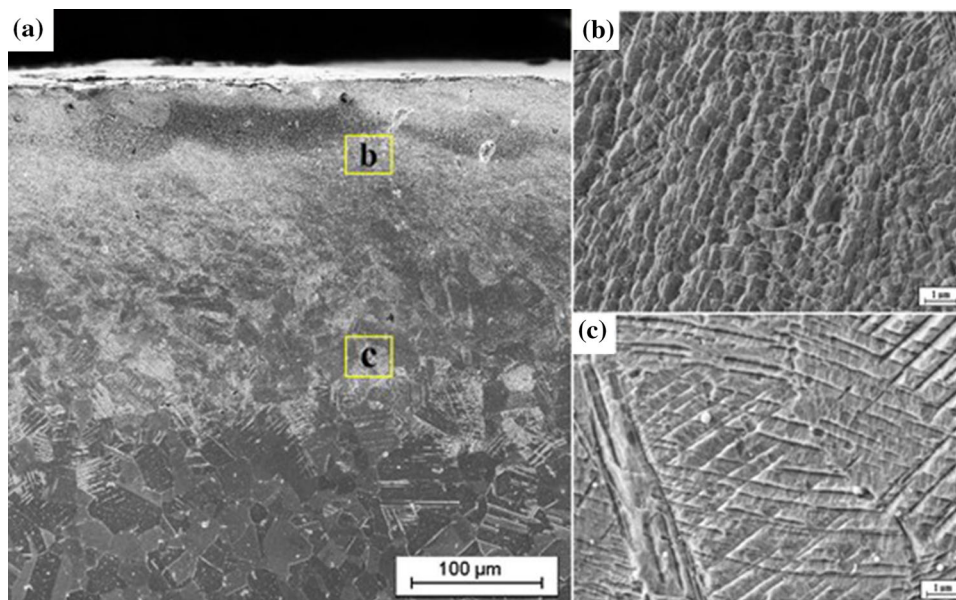

Fig. 1 Cross-sectional SEM images of (a) a shot-peened sample and microstructures at depths of (b) 50 μm and (c) 200 μm
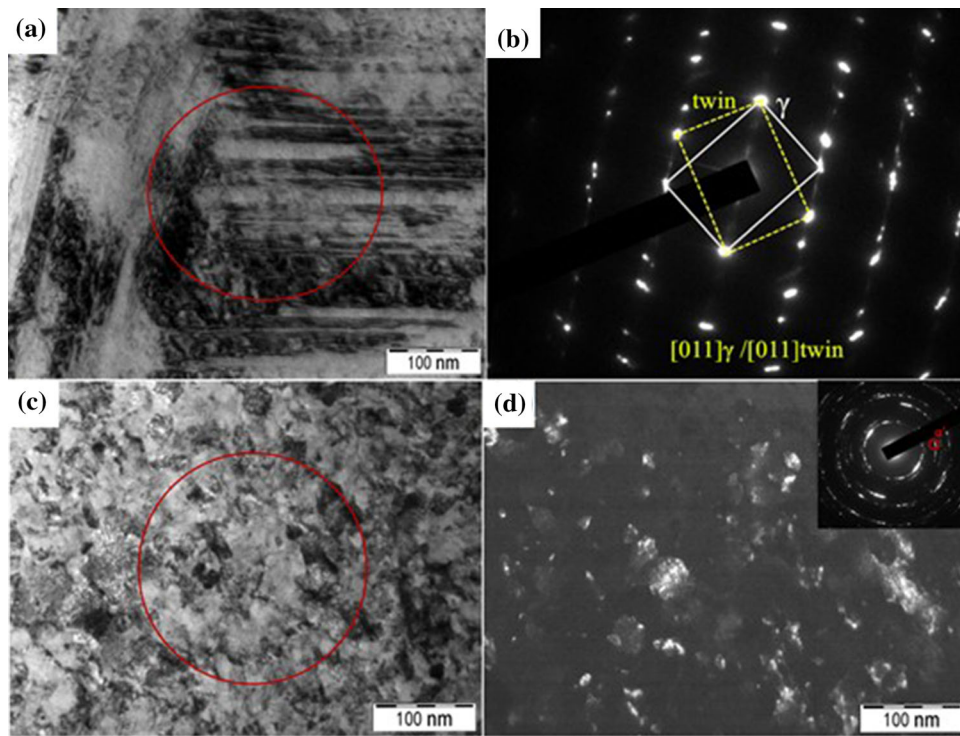
Fig. 2 TEM images of the NT-200 μm sample: (a) bright-field image; (b) selected-area electron diffraction (SAED) pattern of the area in (a) showing austenite and deformation twins with a zone axis of [011]. Nanostructure of the NG-50 μm sample: (c) bright-field image; (d) dark-field image of (c) and the corresponding SAED pattern (inset)
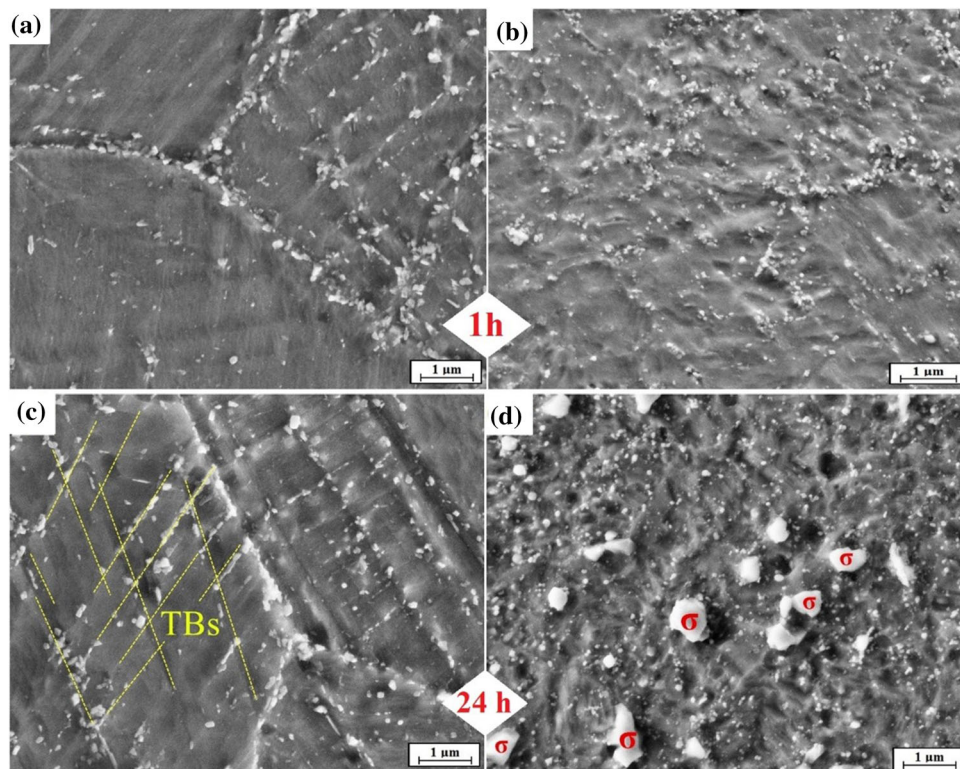

Fig. 3 SEM images of the NT-200 μm sample after aging at 650 °C for (a) 1 h and (c) 24 h. SEM images of the NG-50 μm sample after aging at 650 °C for (b) 1 h and (d) 24 h

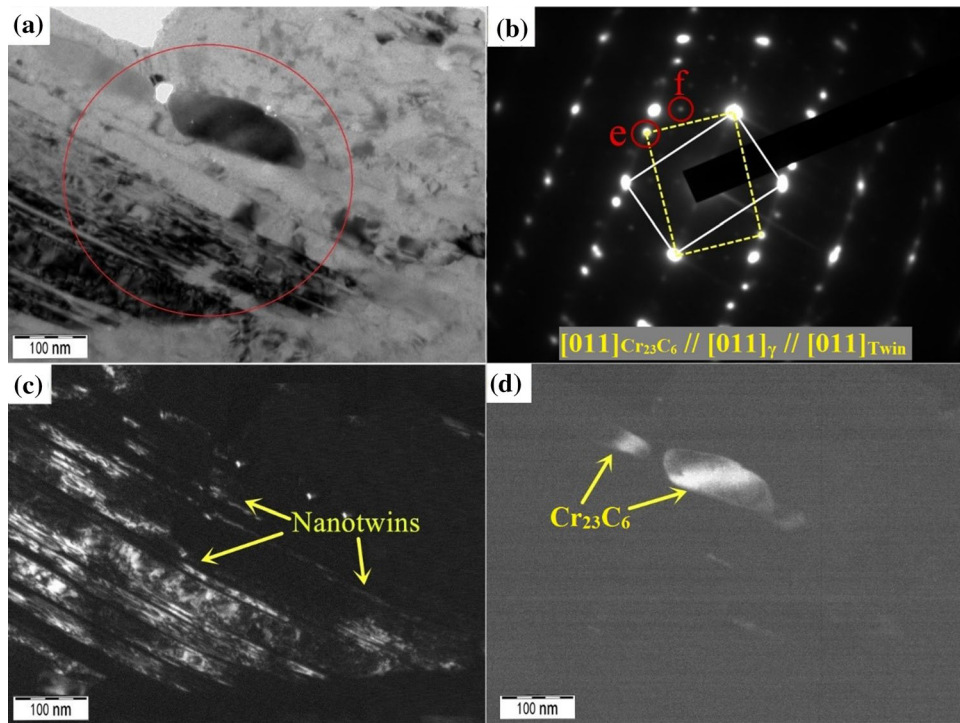**Fig. 4** The microstructure of the NT-200 μm sample after aging at 650 °C for 24 h. (a) Bright-field TEM image of the aged NG-200 μm sample; (b) SAED pattern of the area shown in (a); TEM dark-field images of (c) nano-twins and (d) $Cr_{23}C_6$ carbides
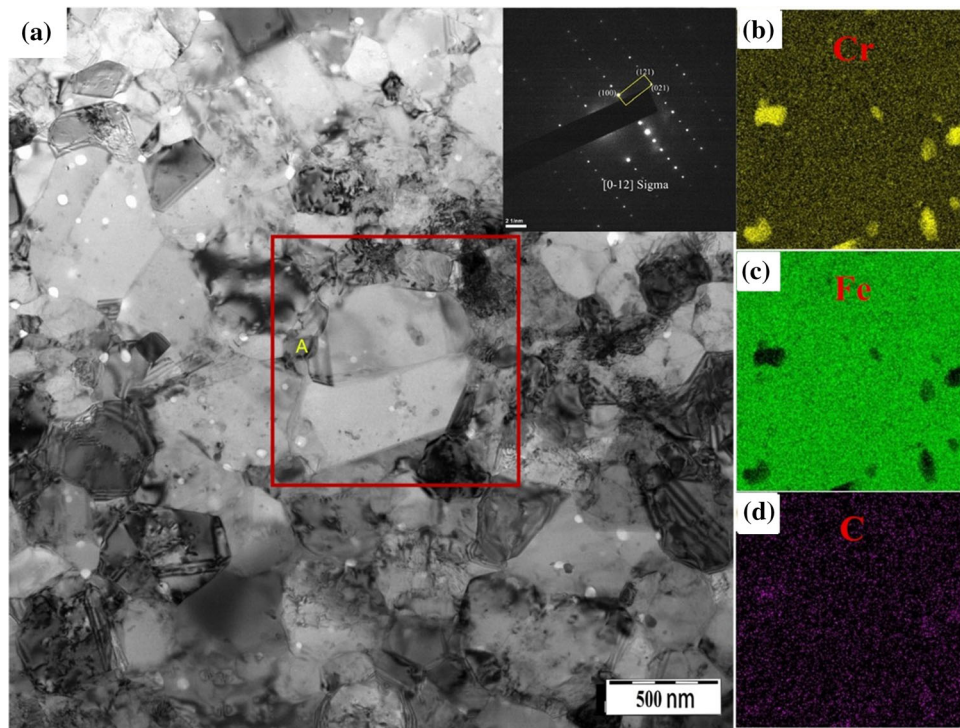

Fig. 5 Microstructure of the NG-50 μm sample after aging at 650 °C for 24 h. (a) Bright-field TEM image of the aged NG-50 μm sample. Inset: SAED pattern of grain 'A'. (b–d) Cr, Fe and C elemental maps of the area within the red rectangle in (a)

TEM dark-field images from the diffraction spots "e" and "f" in the SAED pattern of Fig. 4(b), showing the morphologies of NT and $M_{23}C_6$ carbide, respectively. The NT (in Fig. 4c) was slightly thickened after aging with an average thickness of 35 nm in comparison to that of NT-200 μm samples before aging, as shown in Fig. 2(a). The lath-shaped $M_{23}C_6$ carbide with about 120 nm in length and 45 nm in width is shown in Fig. 4(d). This lath shape of the $M_{23}C_6$ carbide may be

attributed to the limitation of stationary TBs. It can be concluded that the boundaries of deformation twins with massive structural defects not only provide a large number of nucleation active sites for $M_{23}C_6$ carbides, but also limit the carbides to the lath shape in the Super304H SS.

In addition, Fig. 5(a) shows the TEM images of partially static recrystallization of the nano-structures and two sizes of precipitates in the aged NG-50 μm sample at 650 °C for 24 h. The larger precipitates at interfaces of recrystallized and severely deformed grains (in the red rectangular zone of Fig. 5a) are Cr-rich type precipitates, indicated by the mappings of Cr, Fe, and C elements in Fig. 5(b), (c), and (d). Furthermore, the Cr-rich type precipitate (the grain "A" in Fig. 5a) is identified as the sigma phase by SAED pattern analysis (upper inset in Fig. 5a) and EDS results in Table 3.

Over a longer hold time (to 168 h), the $M_{23}C_6$ carbides nucleated in the form of spots (Fig. 3a) and grew into chains along the TBs in the aged NT-200 μm samples (Fig. 6a), but

still in a nano-scale size. In contrast, the size of the sigma phase increased significantly, and many nano-scale $M_{23}C_6$ carbides particles are dispersed in the aged NG-50 μm samples, as shown in Fig. 6(b). Moreover, a TEM image shows that the nano-scale deformed grains completely recrystallized into ultra-fine austenite grain with several coarsened sigma phases precipitated at the triple junctions of recrystallized grain in the aged NG-50 μm samples in Fig. 6(c). The chromium content of sigma phase (the grain "B" in Fig. 6c) increases with aging time according to EDS results in Table 3. The above observations show that the precipitates transformed from the nano-scale $M_{23}C_6$ carbide in the NT-200 μm sample to the coarse σ-phase plus some $M_{23}C_6$ carbides in the NG-50 μm sample during aging at 650 °C for more than 24 to 168 h, which will be discussed later in "Effect of Nano-structured Thermal Stability on the Intergranular Corrosion Behavior" section. The evolution of the nano-structure and formation mechanism of precipitates might influence the IGC behavior of Super304H SS, which would be elaborated in following sections.

3.2 IGC Behavior

3.2.1 DL-EPR Test. Figure 7(a), (b), (c), and (d) shows the DL-EPR curves of the solution-treated, NG-50 μm and NT-200 μm samples after aging at 650 °C for 0.1, 1, 24, and 168 h, respectively. The peak values of the activation current density (i_a) in the DL-EPR are almost remained constant during aging at 650 °C with aging time for three types of samples, while the peak values of the reactivation current density (i_r) vary with aging time, indicating that the consumption of Cr around the
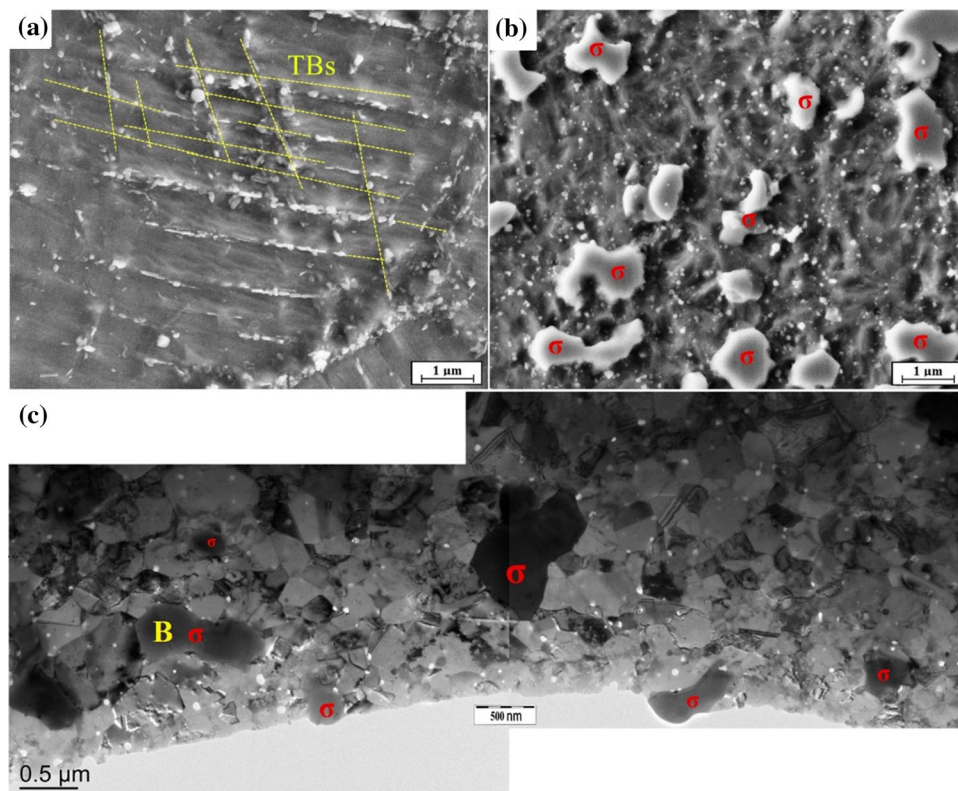
Table 3 The constituent of precipitation phase in Fig. 5(a) and 6(c)

Precipitation code	Chemical composition, wt.%				
	Cr	Ni	Mo	Si	Fe
The grain "A" in Fig. 5(a)	25.86	6.15	0.66	0.43	Bal.
The grain "B" in Fig. 6(c)	28.16	6.54	0.73	0.48	Bal.

Fig. 6 The microstructures of the NG-50 μm and NT-200 μm samples after aging at 650 °C for 168 h. (a, b) The SEM images of the aged NT-200 μm and NG-50 μm samples, respectively; (c) the TEM bright-field image of the aged NG-50 μm sample
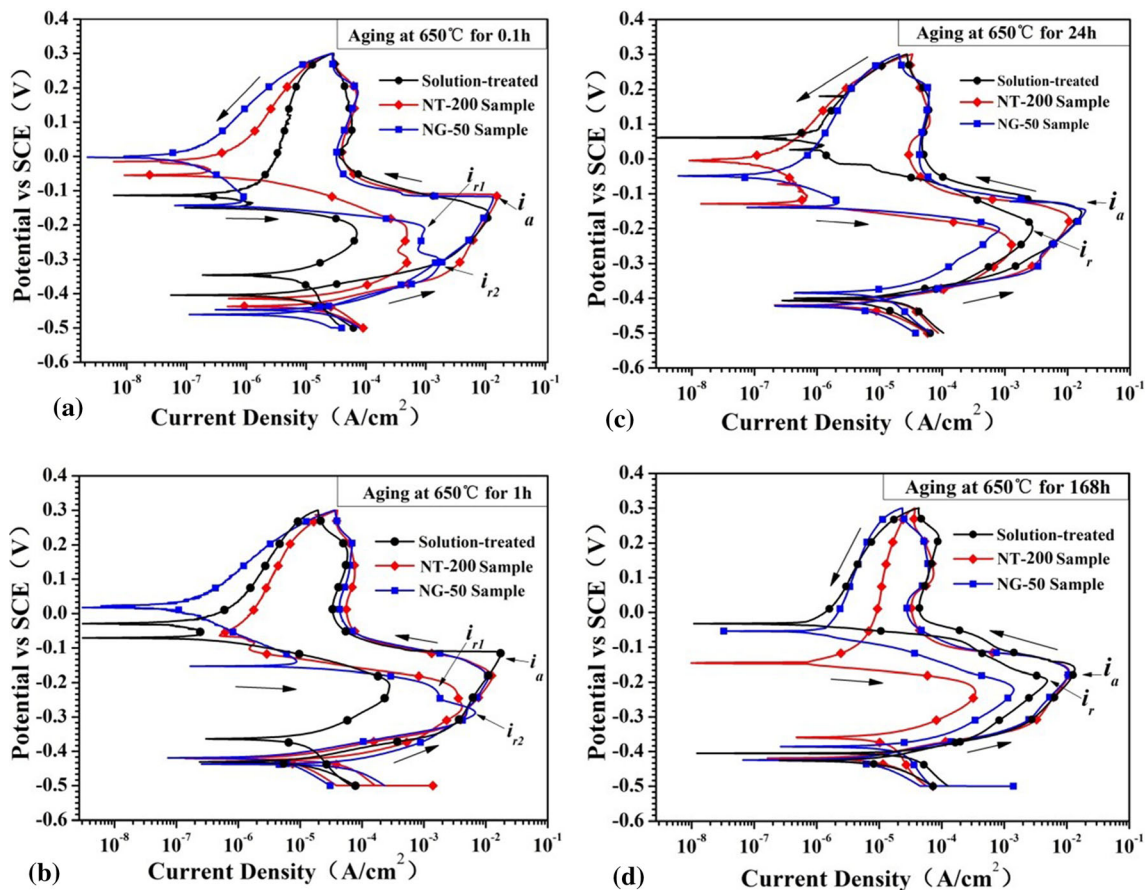
Fig. 7 DL-EPR curves of the solution-treated, NG-50 μm and NT-200 μm samples after aging at 650 °C for various times: (a) 0.1 h; (b) 1 h; (c) 24 h; (d) 168 h. All curves started at the lowest potential (− 0.5 V) and swept up to the top potential (0.3 V) and then back to − 0.5 V

Cr-rich precipitate has changed. After being aged at 650 °C, the typical DL-EPR curves are seen with the significant activation current density peaks and the reactivation current density peaks in the aged samples, which could be attributed to the appearance of Cr-depleted zones, as shown in Fig. 7(a), (b), (c), and (d). Notably, double reactivation current density peaks (Fig. 7a and b) are observed in the DL-EPR in the aged NG-50 μm and NT-200 μm samples because the Cr-depletion regions are caused by two different Cr-rich phases (Ref 18, 33). In such a case, the charge ratio (Q_r/Q_a) is a more accurate formula for indicating dissolution occurring in all Cr-depleted regions (Ref 31).

3.2.2 Intergranular Corrosion Morphologies. The surface morphologies of the aged solution-treated, NG-50 μm and NT-200 μm samples after the DL-EPR tests were observed by SEM to obtain the details of IGC, as shown in Fig. 8. For the solution-treated sample, week IGC is seen at GBs on the early stages of sensitization (Fig. 8a), and as the aging time increases, some evident attacks occur at the GBs with characteristic 'ditch' structure as shown in Fig. 8(b) and (c), respectively. When the NT-200 μm sample was aged for 1 h, severe corrosion was observed at the TBs as well as GBs (as shown in Fig. 8d) since the formation of massive $Cr_{23}C_6$ carbides at these boundaries. As the aging time was extended to 24 h, some narrow ditches were observed at the TBs and GBs in Fig. 8(e). Compared to the NT-200 μm sample aged for 1 h, the corrosion of the sample aged for 24 h (Fig. 8e) has shrunk.

Moreover, very light attacks are observed along the TBs or GBs after aging for 168 h in Fig. 8(f). The above observations indicate that the Cr-depleted zones in the aged NT-200 μm sample are self-healing during aging. For the aged NG-50 μm sample aged for 1 h, more severe IGC (compared to the NT-200 μm sample) was observed on the newly formed GBs, as shown in Fig. 8(g). When the aging time reaches 24 h, multiple IGC (pointed by white arrows) occurs near the σ-phase, as shown in Fig. 8(h), which may be induced by Cr-depleted zones adjacent to the σ-phase. Furthermore, several large corrosion pits (pointed by white arrows) were observed in the NG-50 μm sample (Fig. 8i) aged for 168 h, which were much larger than that in the sample as shown in Fig. 8(h). These SEM results are accordance those of the above DL-EPR tests.

Figure 9 shows the DOS values of three types of samples as a function of aging time, where both NG-50 μm and NT-200 μm samples were aged at 650 °C for 0.1 to 168 h, however, the solution-treated sample was aged at 650 °C for more than 4500 h (Ref 34). The DOS values of both NG-50 μm and NT-200 μm samples increase drastically and reach a maximum after aging for 1 h (the solution-treated sample needs almost 1000 h). Afterward, the DOS values of the NT-200 μm samples decreased rapidly when the time increased from 1 to 168 h. The above result indicates the healing of Cr-depleted zones after 1 h for both NG-50 μm and NT-200 μm samples. However, the trend of the DL-EPR results of the NG-50 μm sample is quite complicated. With the aging time from 1 to
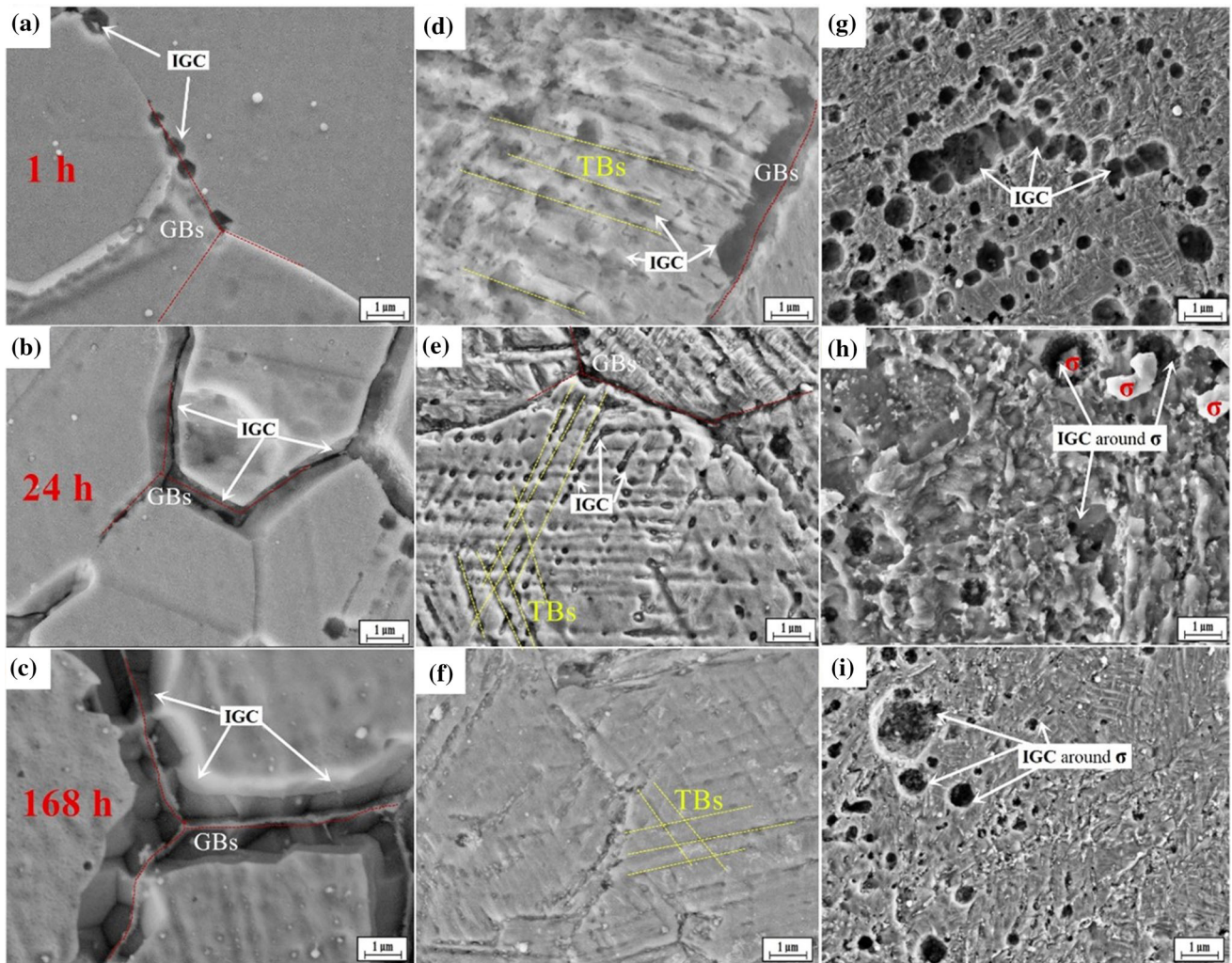
Fig. 8 SEM morphologies of IGC attacks after DL-EPR tests of the solution-treated samples (a–c), NT-200 μm samples (d–f) and NG-50 μm samples (g–i) aging at 650 °C for 1, 24 and 168 h, respectively
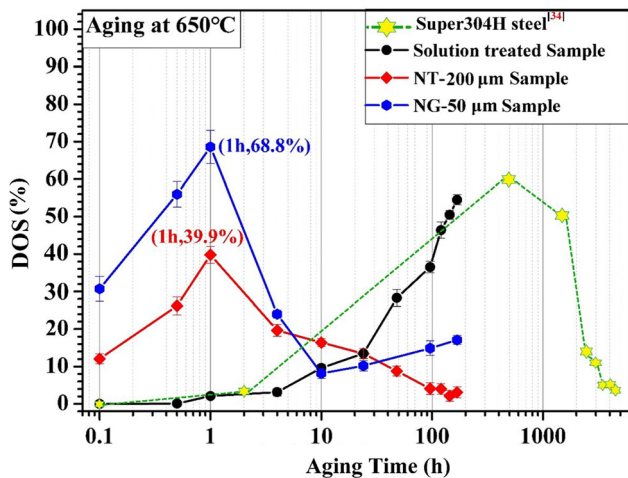

Fig. 9 Dependence of the DOS values on the aging time of NG-50 μm and NT-200 μm samples after aging at 650 °C, in comparison to that of the Super304H SS aging at 650 °C for more than 4000 h (Ref 34)

10 h, the DOS values of the NG-50 μm samples decrease to the lowest level of 9% at 10 h, which is faster than those of the NT-200 μm samples. Afterward, the DOS values turn to increase again, reaching 10.2 and 18.1% at 24 and 168 h of aging, respectively. The difference in the IGC behavior between the two SPed samples is mainly due to their different nano-structures with different character grain boundaries, which will be discussed later in "Discussion" section.

4. Discussion

4.1 Effect of Nano-structured Thermal Stability on the Intergranular Corrosion Behavior

According to the literature (Ref 34), the main strengthening phases are Nb(C,N), NbCrN and Cu-rich phase in the Super304H SS. In this research, the refinement of Super304H SS into nano-structures by high-rate SP will inevitably bring many defects, including high density of dislocations (Ref 35, 36) which act as the diffusion channels for Cr atoms, newly formed GBs of deformation twins (Ref 37), α′-martensite and
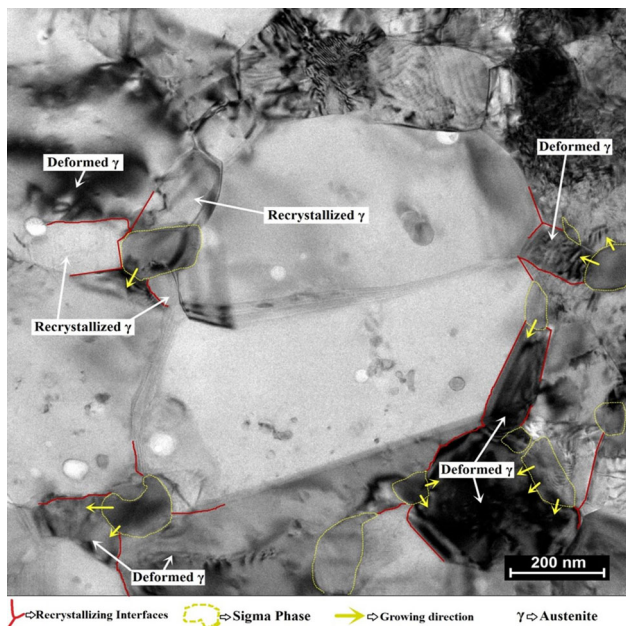
Fig. 10 The microstructure of the NG-50 μm samples after aging at 650 °C for 24 h. The magnification of the red rectangular zone in Fig. 5(a)

subgrains (Ref 38), which are active sites that facilitate the precipitation of carbides. As a result, they could accelerate the precipitation of massive chromium carbides during the subsequent aging (see Fig. 3a and b), thereby deteriorating the IGC resistance of nano-structured Super304H after aging at 650 °C for 1 h, as indicated in Fig. 8(d) and (g). In addition, the increase of strain level will increase the number of high-energy interfaces and provide more active sites for chromium carbides precipitation, which will lead to a higher IGCS of the NG-50 μm sample than that of the NT-200 μm sample during the sensitization period, as demonstrated in Fig. 9.

The healing of Cr-depletion zones in the nano-structured Super304H SS also could be effectively accelerated because the Cr-depletion zones can quickly obtain Cr atoms from the adjacent nano-structure matrix owing to its high-diffusion rate in the nano-structures. Therefore, the DOS values of the NG-50 μm and NT-200 μm samples reach their peak at the aging time of 1 h, and then begin to decline because the Cr atoms diffuse from the adjacent nano-structure to the Cr-depletion regions. As the aging time increases from 1 to 10 h, the higher dislocation density due to higher strain level in the nano-grained structure (NG-50 μm) sample results in a relatively rapid decrease of DOS value (Fig. 9). However, the DOS value of the NG-50 μm sample is again positively correlated with the aging time of 10 to 168 h, which may be due to the nucleation and growth of the Cr-rich intermetallic σ-phase.

Note that aging the NG-50 μm sample for more than 10 h induced the recrystallization of nano-grained structures and the nucleation of σ-phases. However, for the solution-treated Super304H SS, no σ-phase was found in the available long-term creep (over 4500 h at 650 °C) samples (Ref 34). The precipitation of σ-phase in AISI-304 stainless steel requires not only high-energy interfaces, but also enhanced chemical driving force of Cr atoms (Ref 39, 40). According to the literature (Ref 41), the lowest nucleation energy of σ-phase in the highly deformed austenitic stainless steel is supposed at the

interfaces between deformed grains and recrystallizing domains (recrystallizing interfaces) during aging. This interface can also offer a high-diffusion rate of the solute atoms from the deformed austenitic matrix to promote the nucleation growth. Hence, the recrystallizing interfaces are preferential sites for the nucleation and growth of σ-phases in the deformed austenite steel, and the fast precipitation of σ-phases in the nano-structured Super304H SS should be closely related to its recrystallization process.

In this research, NG structures are unstable and prone to recrystallize during the aging process, which would offer great numbers of preferential sites for the precipitation of σ-phases. Figure 10 shows the TEM images of partially static recrystallization of the nano-structures and the size of σ-phases are still at the nano-meter level in the aged NG-50 μm sample. Meanwhile, the σ-phases are mostly observed at recrystallizing interfaces (indicated by red line) but scarcely at the only deformed grain boundaries. This is because it is at an early stage of recrystallisation-induced σ precipitation. Over a longer hold time (to 168 h), the size of the σ-phases increased significantly to several microns by absorbing or encircling the recrystallized grain during recrystallization, as shown in Fig. 6(c). Moreover, the sigma phase is chromium-rich phase (Fig. 5b), which can bring about chromium depletion regions after precipitation at the interfaces, and then IGC is prone to occur under some conditions. Hence, IGC occurred near the σ-phase in the NG-50 μm sample after aging at 650 °C for a shorter time as shown in Fig. 8(h). During aging at 650 °C for a longer time, the σ-phases become coarsen (the Fig. 3d and 6b) and lead to form wider chromium depletion regions around the σ-phases. However, the recrystallized domains with low dislocation density have no enough channels to transfer Cr atoms to restore the chromium depletion regions. Therefore, the DOS value of the NG-50 μm sample rises again with aging time, as demonstrated in Fig. 9. In a word, the NG structure with poor thermal stability during the aging process would seriously reduce the IGC resistance of nano-structured Super304H SS.

4.2 Enhanced Thermal Stability and IGC Resistance in the Nano-twinned Super304H SS

The above analysis shows that the thermal stability of the microstructure is the key factor to the IGC behavior of nano-structured Super304H SS during aging. If the nano-structure is thermal stable and hard to recrystallize, Cr-depletion zones could rapidly obtain Cr atoms diffused from the adjacent matrix because of the high-diffusion rate in nano-structure during aging. As the diffusion rate of Cr atoms from the nano-structured matrix to the Cr-depletion zones is higher than the Cr-depletion rate induced by the precipitation of Cr-rich phases, the Cr-depletion zones will be replenished gradually and IGC resistance of the material will be restored (Ref 16).

As shown in Fig. 2(a) and 4(a), the NT structures in the NG-200 μm samples almost remain unchanged during aging at 650 °C. The experimental results show that the thermal stability of the NT structures is superior to that of the NG structures in the nano-structured Super304H SS. This difference in thermal stability results from the difference between the excess energy stored in GBs of the NG structures and that in TBs of the NT structures. According to the literature (Ref 42), TBs are usually believed to be a special coherent boundary with a very low excess energy, and the energy stored at TBs is an order of

magnitude lower than at high-angle GBs. Although the excess energy of TBs induced by plastic deformation at high-strain rates could be increased by introducing high density of dislocations, the excess energy of deformed TBs is still far lower than that of high-angle GBs (Ref 21, 26). Hence, the excess energy stored in the NT structures is far lower than that in the NG structures. Moreover, other studies have found that the deformed NT in AISI-304 stainless steel can even withstand heat treatment up to 800 °C (Ref 27). Therefore, the nano-twinned Super304H SS exhibits a high thermally stable during aging at 650 °C.

It should be mentioned that a larger amount of $M_{23}C_6$ precipitates formed along deformed TBs (Fig. 3a) at the beginning of aging and leaded to an increase in the DOS value. This is contradictory to the percolation theory (Ref 43) that annealing twins in grain boundary engineering (GBE) have better resistance to IGC due to low energy of coincident site lattices and low probability of precipitates nucleation, and the other research work (Ref 22) found that high density deformed TBs networks in the twinned 304 stainless steel can inhibit the precipitation of $M_{23}C_6$ carbides. Such contradictory results may be due to two special functions of the nano-twinned Super304H SS. The first is the carbon content, which is a dominant factor. High-carbon content can improve the precipitation kinetics of chromium-rich carbides in the early stage of sensitization (Ref 44). The Super304H SS was based on the 304H SS, which was developed by increasing the content of carbon and adding elements such as copper, niobium, and nitrogen (Ref 1). Hence, the carbon content of Super304H SS ($> 0.10\%$ in this work) can significantly promote the precipitation of $M_{23}C_6$ carbides in the NT structure. The second is the ledge of the deformation twins, which is an active site with respect to the regular crystal structure. It contains a lot of structural defects caused by deformation, which is conducive to the precipitation of chromium carbide (Ref 37, 38). The deformed TBs are thereby providing a large number of active sites for nucleation of carbides and accelerating the precipitation of massive $M_{23}C_6$ carbides during aging in 1 h.

However, the nano-twinned Super304H SS not only promotes the precipitation of $M_{23}C_6$ carbides, but also restricts the growth of the precipitate, as shown in Fig. 3(a), (c) and 6(a). Hence, as the increasing of aging time, the superior thermal stability and high Cr diffusion rate in the NT structure would result in the fast healing of the Cr-depleted zones during aging at 650 °C, and ultimately recovering the IGC resistance of the nano-structured Super304H SS, as shown in Fig. 9. Therefore, the NT structure with superior stability during the aging process could enhance the IGC resistance of nano-structured Super304H SS, following the self-healing mechanism instead of inhibiting carbide precipitation.

The above results reveal that the surface NT structure is a promising way to eliminate the high IGCS of the high-carbon Super304H SS but its working temperature (650 °C) could promote σ-phase nucleation happening at the recrystallizing NG structure, which must be inhibited in practical applications because of its deteriorative effect on the IGC resistance of Super304H SS. Therefore, the high-rate SP strain levels must be controlled to be lower than the saturation value, which could result in the transformation of the grain refinement mechanism from twinning to dislocation slip, to develop an ideal NT structure to further enhance thermal stability and IGC resistance as well as to avoid recrystallization-induced σ-phase precipitation in the Super304H SS.

5. Conclusions

(1) The primary microstructure varies from the nano-twins to the nano-grains following the grain refinement mechanism changes from twinning to dislocation slip with increasing strain level, which resulted in the main precipitates transformed from the nano-scale $M_{23}C_6$ carbide in the NT-200 μm sample to the coarsening σ-phase plus some $M_{23}C_6$ carbides in the NG-50 μm sample after aging at 650 °C for various times.

(2) The NG structures with poor thermal stability in the surface of the NG-50 μm samples can accelerate the precipitation of the σ-phase at the recrystallizing interfaces, thereby deteriorating the IGC resistance of nano-structured Super304H SS after long-time aging at 650 °C.

(3) The IGC behavior of the NT-200 μm sample is controlled by the formation of nano-scale $M_{23}C_6$ and then fast healing of Cr-depletion region around $M_{23}C_6$ precipitation during the aging process. Therefore, the NT structure with superior thermal stability could enhance the IGC resistance of nano-structured Super304H SS, followed the self-healing mechanism instead of inhibiting carbide precipitation.

(4) The high-rate SP strain levels must be controlled to be lower than the saturation value, which results in the transformation of the grain refinement mechanism from twinning to dislocation slip, to develop an ideal NT structure to further enhance thermal stability and IGC resistance as well as to avoid recrystallization-induced σ-phase precipitation in the Super304H SS.

References

1. Y. Sawaragi, N. Otsuka, H. Senba, and S. Yamamoto, Properties of a New 18-8 Austenitic Steel Tube (SUPER 304H) for Fossil Fired Boilers After Service Exposure with High Elevated Temperature Strength, *Sumitomo Search*, 1994, **56**, p 34–43

2. A. Iseda, H. Okada, H. Semba, and M. Igarashi, Long Term Creep Properties and Microstructure of Super304H, TP347HFG and HR3C for A-USC Boilers, *Energy Mater.*, 2007, **2**, p 199–206

3. J.H. Kim, D.I. Kim, S. Suwas, E. Fleury, and K.W. Yi, Grain-Size Effects on the High-Temperature Oxidation of Modified 304 Austenitic Stainless Steel, *Oxid. Met.*, 2013, **79**, p 239–247

4. S. Swaminathan, N.G. Krishna, and D.I. Kim, Characteristics of Oxide Scale Formed on Cu-Bearing Austenitic Stainless Steel during Early Stages of High Temperature Oxidation, *Appl. Surf. Sci.*, 2015, **353**, p 29–39

5. X.M. Li, Y. Zou, Z.W. Zhang, and Z.D. Zou, Microstructure Evolution of a Novel Super304H Steel Aged at High Temperatures, *Metall. Trans. A*, 2010, **51**, p 305–309

6. D.B. Park, S.M. Hong, K.H. Lee, M.Y. Lee, J.Y. Suh, S.C. Lee, and W.S. Jung, High-Temperature Creep Behavior and Microstructural Evolution of an 18Cr9Ni3CuNbVN Austenitic Stainless Steel, *Mater. Charact.*, 2014, **93**, p 52–61

7. Y. Gao, C.L. Zhang, X.H. Xiong, Z.J. Zheng, and M. Zhu, Intergranular Corrosion Susceptibility of a Novel Super304H Stainless Steel, *Eng. Fail. Anal.*, 2012, **24**, p 26–32

8. Y. Samaragi and F. Nasuyama, Properties After Service Exposure of a New 18-8 Austenitic Stainless Steel Tube (0.1C-18Cr-9Ni-3Cu-Nb, N)

with High Elevated Temperature Strength for Fossil Fired Boilers, *Met. Mater. Soc. (TMS)*, 1993, **420**, p 179–186

9. R.W. Swinderman and P.J. Maziasz, The Mechanical and Microstructural Stability of Austenitic Stainless Steels Strengthened by MC-Forming Elements, in *5th International Conference on Creep of Materials, Ohio, USA* (ASM, 1992), p 33–42

10. T. Kan, Y. Sawaragi, Y. Yamadera, and H. Okada, Properties and Experiences of a New Austenitic Stainless Steel Super304H (0.1C-18Cr-9Ni-3Cu-Nb-N) for Boiler Tube Application, in *Proceedings of the 6th Leige Conference* (Forschingszentrum, 1998), p 60

11. I. Sen, E. Amankwah, and N.S. Kumar, Microstructure and Mechanical Properties of Annealed SUS 304H Austenitic Stainless Steel with Copper, *Mater. Sci. Eng. A*, 2011, **528**, p 4491–4499

12. J. Cao, Y. Gong, K. Zhu, Z.G. Yang, X.M. Luo, and F.M. Gu, Microstructure and Mechanical Properties of Dissimilar Materials Joints Between T92 Martensitic and S304H Austenitic Steel, *Mater. Des.*, 2011, **32**, p 2063–2070

13. Y. Zhang, L. Zhu, A. Qi, and Z. Lu, Microstructural Evolution and the Effect on Mechanical Properties of S30432 Heat-Resistant Steel during Aging at 650 °C, *ISIJ Int.*, 2010, **50**, p 596–600

14. X.M. Li, Y. Zou, Z.W. Zhang, and Z.D. Zou, Intergranular Corrosion of Weld Meld of Super Type 304H Steel during 650 °C Aging, *Corrosion*, 2012, **68**, p 379–387

15. R.K. Wang, Z.J. Zheng, and Y. Gao, Effect of Shot Peening on the Intergranular Corrosion Susceptibility of a Novel Super304h Austenitic Stainless Steel, *J. Mater. Eng. Perform.*, 2015, **25**, p 20–28

16. G.S. Bai, S.P. Lu, D.H. Li, and Y.Y. Li, Intergranular Corrosion Behavior Associated with Delta-Ferrite Transformation of Ti-Modified Super304H Austenitic Stainless Steel, *Corros. Sci.*, 2015, **90**, p 347–358

17. C.L. Zhang, X.H. Xiong, S.B. Ping, and Y. Gao, Influence of Chemical Composition on the Intergranular Corrosion Susceptibility of Super304H Austenitic Heat-Resistant Steel, *Br. Corros. J.*, 2014, **49**, p 624–632

18. R.K. Wang, Z.J. Zheng, Q.W. Zhou, and Y. Gao, Effect of Surface Nanocrystallization on the Sensitization and Desensitization Behavior of Super304H Stainless Steel, *Corros. Sci.*, 2016, **111**, p 728–741

19. I. Altenberger, E.A. Stach, G.Y. Liu, R.K. Nalla, and R.O. Ritchie, An In Situ Transmission Electron Microscopy Study of the Thermal Stability of Near-Surface Microstructures Induced by Deep Rolling and Laser-Shock Peening, *Scr. Mater.*, 2003, **48**, p 1593–1598

20. C.H. Manish and F.A. Mohamed, Investigation of Low Temperature Thermal Stability in Bulk Nanocrystalline Ni, *Mater. Sci. Eng. A*, 2006, **427**, p 7–15

21. X. Zhang and A. Misra, Superior Thermal Stability of Coherent Twin Boundaries in Nanotwinned Metals, *Scr. Mater.*, 2012, **66**, p 860–865

22. A.Y. Chen, W.F. Hu, and D. Wang, Improving the Intergranular Corrosion Resistance of Austenitic Stainless Steel by High Density Twinned Structure, *Scr. Mater.*, 2017, **130**, p 264–268

23. M. Lale and K. Farzad, Suppression of Chromium Depletion and Sensitization in Austenitic Stainless Steel by Surface Mechanical Attrition Treatment, *Mater. Lett.*, 2011, **65**, p 1935–1937

24. D. Sagapuram, Z. Wang, and C. Saldana, Thermal Stability of Nanotwinned and Nanocrystalline Microstructures Produced by Cryogenic Shear Deformation, *Philos. Mag.*, 2014, **94**, p 3413–3430

25. C. Saldana, T.G. Murthy, M.R. Shankar, E.A. Stach, and S. Chandrasekar, Stabilizing Nanostructured Materials by Coherent Nanotwins and Their Grain Boundary Triple Junction Drag, *Appl. Phys. Lett.*, 2009, **94**, p 219–325

26. T.H. Sinha and Y. Kulkarni, Anomalous Deformation Twinning in fcc Metals at High Temperatures, *J. Appl. Phys.*, 2011, **109**(11), p 114–135

27. F.K. Yan, G.Z. Liu, N.R. Tao, and K. Lu, Strength and Ductility of 316L Austenitic Stainless Steel Strengthened by Nano-scale Twin Bundles, *Acta Mater.*, 2012, **60**, p 1059–1071

28. H.L. Chan, H.H. Ruan, A.Y. Chen, and J. Lu, Optimization of the Strain Rate to Achieve Exceptional Mechanical Properties of 304 Stainless Steel Using High Speed Ultrasonic Surface Mechanical Attrition Treatment, *Acta Mater.*, 2010, **58**, p 5086–5096

29. A.T. Krawczynska, M. Gloc, and K. Lublinska, Intergranular Corrosion Resistance of Nanostructured Austenitic Stainless Steel, *J. Mater. Sci.*, 2013, **48**, p 4517–4523

30. ISO12732, *Corrosion of Metals and Alloys. Electrochemical Potentiokinetic Reactivation Measurement Using the Double Loop Method (Based on Cihal's Method)*, ISO, Geneva, 2006

31. K.S. de Assis, F.V.V. de Sousa, M. Miranda, I.C.P. Margarit-Mattos, V. Vivier, and O.R. Mattos, Assessment of Electrochemical Methods Used on Corrosion of Superduplex Stainless Steel, *Corros. Sci.*, 2012, **59**, p 71–80

32. A.Y. Chen, H.H. Ruan, J. Wang, H.L. Chan, Q. Wang, Q. Li, and J. Lu, The Influence of Strain Rate on the Microstructure Transition of 304 Stainless Steel, *Acta Mater.*, 2011, **59**, p 3697–3709

33. V. Kain, K. Chandra, K.N. Adhe, and P.K. De, Detecting Classical and Martensite-Induced Sensitization Using The Electrochemical Potentiokinetic Reactivation Test, *Corrosion*, 2005, **61**, p 587–593

34. X. Huang, Q.W. Zhou, W. Wang, W.S. Li, and Y. Gao, Microstructure and Property Evolutions of a Novel Super304H Steel during High Temperature Creeping, *Mater. High Temp.*, 2018, **35**, p 438–450

35. A. Pardo, M.C. Merino, A.E. Coy, F. Viejo, M. Carboneras, and R. Arrabal, Influence of Ti, C and N Concentration on the Intergranular Corrosion Behaviour of AISI, 316Ti and 321 Stainless Steels, *Acta Mater.*, 2007, **55**, p 2239–2251

36. E.A. Trillo, R. Beltran, J.G. Maldonado, R.J. Romero, and L.E. Murr, Combined Effects of Deformation (Strain and Strain State), Grain Size and Carbon Content on Carbide Precipitation and Corrosion Sensitization in 304 Stainless Steel, *Mater. Charact.*, 1995, **35**, p 99–112

37. E.C. Bain, R.H. Aborn, and J.B. Rutherford, The Nature and Prevention of Intergranular Corrosion in Austenitic Stainless Steels, *Trans. ASST*, 1993, **21**, p 481–509

38. A.H. Advani, L.E. Murr, D.G. Atteridge, and R. Chelakara, Mechanisms of Deformation-Induced Grain Boundary Chromium Depletion (Sensitization) Development in Type 316 Stainless Steels, *Metall. Mater. Trans. A*, 1991, **22**, p 2917–2934

39. L.K. Singhal and J.W. Martin, The Formation of Ferrite and Sigma-Phase in Some Austenitic Stainless Steels, *Acta Metall.*, 1968, **16**, p 1441–1451

40. B. Weiss and R. Stickler, Phase Instabilities during High Temperature Exposure of 316 Austenitic Stainless Steel, *Metall. Trans. A*, 1972, **3**, p 851–860

41. F. Abe, H. Araki, and T. Noda, Discontinuous Precipitation of σ-Phase during Recrystallisation in Cold Rolled Fe-10Cr-30Mn Austenite, *Mater. Sci. Technol.*, 1988, **4**, p 885–893

42. Y. Wei, Y. Li, L. Zhu, Y. Liu, X. Lei, G. Wang, Y. Wu, Z. Mi, J. Liu, H. Wang, and H. Gao, Evading the Strength–Ductility Trade-Off Dilemma in Steel through Gradient Hierarchical Nanotwins, *Nat. Commun.*, 2014, **5**, p 1–8

43. M. Frary and C.A. Schuh, Grain Boundary Networks: Scaling Laws, Preferred Cluster Structure, and Their Implications for Grain Boundary Engineering, *Acta Mater.*, 2005, **53**, p 4323–4335

44. C.L. Briant and A.M. Ritter, The Effects of Deformation Induced Martensite on the Sensitization of Austenitic Stainless Steels, *Metall. Trans. A*, 1980, **11**, p 2009–2017